

# Pseudo-random masks for angular alignment

CRISTINA M. GÓMEZ-SARABIA,<sup>1</sup> LUIS M. LEDESMA-CARRILLO,<sup>2</sup> CIPRIANO GUZMÁN-CANO,<sup>2</sup>  
MIGUEL TORRES-CISNEROS,<sup>2</sup> RAFAEL GUZMÁN-CABRERA,<sup>3</sup> AND JORGE OJEDA-CASTAÑEDA<sup>2,\*</sup>

<sup>1</sup>Digital Arts Department, Engineering Division, University of Guanajuato, 36885 Guanajuato, Mexico

<sup>2</sup>Electronics Department, Engineering Division, University of Guanajuato, 36885 Guanajuato, Mexico

<sup>3</sup>Electrical Engineering, Engineering Division, University of Guanajuato, 36885 Guanajuato, Mexico

\*Corresponding author: [jojedacas@ugto.mx](mailto:jojedacas@ugto.mx)

Received 16 June 2017; revised 17 July 2017; accepted 29 August 2017; posted 30 August 2017 (Doc. ID 298170); published 27 September 2017

We present an alignment technique that exploits angular correlations by employing a pair of masks, which encode in an angular format pseudo-random sequences. The angular correlator generates peaked irradiance distributions on-axis, provided that the elements of the pair are aligned. Otherwise, the on-axis irradiance distribution decreases to a minimum value. Since the proposed angular correlator is independent of the lateral magnification, it is useful for testing the performance of varifocal lenses. A merit function describes the tolerance to focus errors associated with the location of a small size detector. We use linearly polarized films for showing that the technique also works well with broad band light. © 2017 Optical Society of America

**OCIS codes:** (070.6110) Spatial filtering; (130.6010) Sensors; (070.4550) Correlators; (110.1220) Apertures; (120.4570) Optical design of instruments; (070.2615) Frequency filtering.

<https://doi.org/10.1364/AO.56.007869>

## 1. INTRODUCTION

Presently, there are several competing technologies for implementing varifocal lenses [1–5]. Among other applications, varifocal lenses can be useful for implementing non-conventional zoom systems [6–10]. As the magnification changes, the zoom systems must produce images that are neither shifted nor rotated.

Hence, one needs an alignment technique for testing that the images remain at fixed locations, while the magnification changes. For this task, it is convenient to employ fiducial marks, which have low sensitivity to lateral magnification, but high sensitivity to angular mismatching.

In Fig. 1, we depict the use of a varifocal lens for imaging with variable lateral magnification,  $|M| > 1$ , two planes that are separated by a fixed distance  $T$ . At the input plane, we place a mask with amplitude transmittance equal to  $P_1(\rho, \phi)$ . Just behind the image plane, we place a second mask, whose complex amplitude transmittance is equal to  $P_1(\rho, \phi - 180^\circ)$  for compensating the geometrical inversion caused by the lens. An additional lens is used for focusing on-axis the irradiance distribution, which is recorded using a small size detector.

In what follows, we show that optical system in Fig. 1 is an angular correlator. As a working hypothesis, we assume that the performance of the angular correlator is improved by employing pseudo-random sequences in an angular format. Hence, we discuss the design of mask encoding in the angular format, known as Barker sequences [11].

For properly framing our proposal, we note that Moiré patterns are useful for detecting subtle displacements or local

distortions if one uses two (or more) periodic patterns. Since moiré patterns can be recorded under noncoherent illumination, the moiré techniques have low sensitivity to noise [12,13].

On the other hand, optical correlations can be exploited for implementing several metrological devices. This field can be traced back to the Hanbury Brown and Twiss effect [14] and to the pioneering uses of speckle interferometry [15,16]. We note that digital image correlations also work under noncoherent illumination [17,18].

Optical correlations employing pseudo-random sequences [19] find applications for sharpening Moiré fringes [20,21] and for generating novel periodic patterns [22,23]. Interestingly, pseudo-random sequences are useful for reducing the presence of Moiré patterns [24,25], and, rather recently, pseudo-random bit sequences have been used for surpassing the Shannon–Nyquist sampling ratio [26,27].

Here, we unveil the use of a pair of optical masks that encode angular Barker pseudo-random sequences for implementing an angular correlator. We show that the angular correlations generate highly peaked irradiance distributions on-axis, provided that the pair is angularly aligned. Otherwise, the on-axis irradiance distribution decreases to a minimum value. Furthermore, we note that variations on the correlation peaks are useful for identifying geometrical distortions on the masks. As a proof of principle, we use linearly polarized films for showing that the technique also works well with broad band light.

In Section 2, we apply the McCutchen theorem [28,29] for describing the collected irradiance behind the pair of angularly

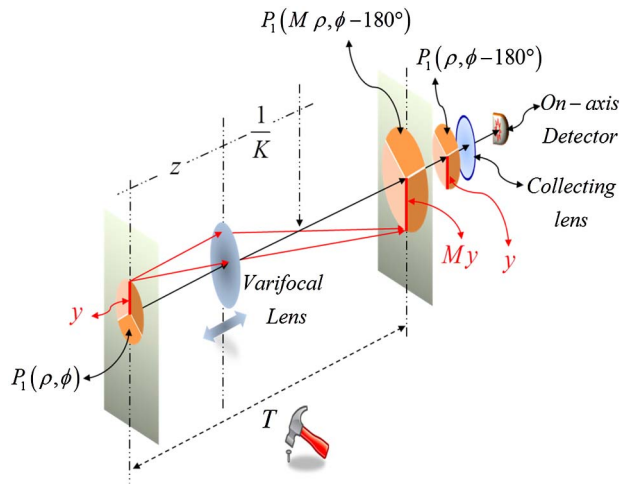


**Fig. 1.** Schematics of an angular correlator. Varifocal lens images with variable lateral magnification  $|M| > 1$ , two planes that are separated by a fixed distance  $T$ . At the input plane, we locate a mask, whose amplitude transmittance is  $P_1(\rho, \phi)$ . Just behind the image plane, we place a second mask, whose amplitude transmittance is  $P_1(\rho, \phi - 180^\circ)$ . An additional lens is used for focusing on-axis the overall irradiance distribution.

coded masks. In Section 3, we discuss the designing steps for proposing a pair of angular masks encoding nested Barker sequences. In Section 4, we discuss the use of a merit function for analyzing the tolerance to focus error of the detector. In Section 5, we describe the use of two orthogonal polarization states for implementing, under noncoherent illumination, an angular version of the Barker sequence. In Section 6, as a proof of principle, we report preliminary experimental results. Finally, in Section 7, we summarize our contribution.

## 2. BASIC THEORY

In Fig. 2, we illustrate other possible configurations for using the proposed pair of masks. The optical setups in Fig. 2 depict the idea that the proposed masks can be thought of as a spatial filter in the Fourier domain. However, the relevant feature is collecting the overall irradiance distribution that is focused on-axis. We note that in Fig. 2, the collection is done by using either a single lens or two lenses. In Fig. 1, a final lens is needed for focusing, on-axis, the overall irradiance distribution.

We are interested in evaluating the complex amplitude transmittance behind the pair of masks, after introducing an angular mismatch between the elements of the pair;

$$P(\rho, \phi; \alpha) = P_1\left(\rho, \phi + \frac{\alpha}{2}\right) P_1\left(\rho, \phi - \frac{\alpha}{2}\right). \quad (1)$$

In Eq. (1), we denote  $(\rho, \phi)$  as the polar coordinates at planes containing the masks. Also in Eq. (1), the Greek letter  $\alpha$  denotes an in-plane rotation angle between the elements of the pair.

Next, we recognize the following result that incorporates a possible error  $z$  on the axial location of the small size detector. In the paraxial regime, the complex amplitude transmittance

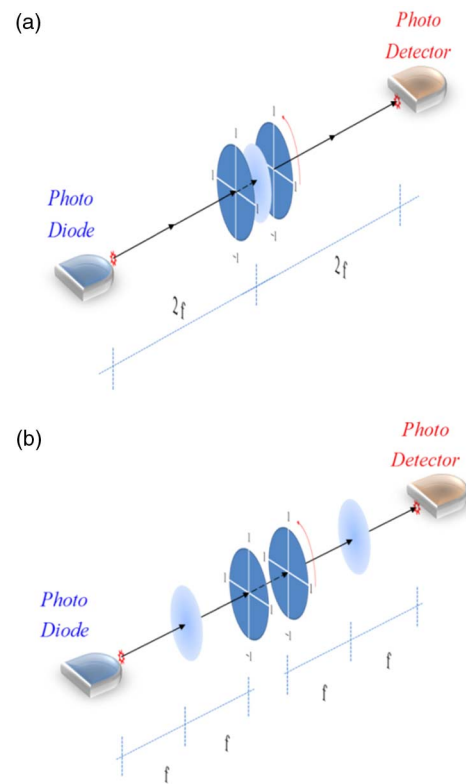


**Fig. 2.** Optical setups that can be employed for collecting the irradiance distribution behind  $t$ , a pair of angular coded masks. Here, the pair of angularly coded masks is located at the Fraunhofer plane: (a) the optical setup uses a single lens; (b) the optical setup is the classical two-lens optical processor.

at the detector plane is obtained by taking the following two-dimensional (2D) Fourier transform:

$$p(r, \theta, z; \alpha) = \int_0^\infty \int_0^{2\pi} P(\rho, \phi; \alpha) \exp\{-i\pi\lambda z \rho^2\} \times \exp\{i2\pi r \rho \cos(\theta - \phi)\} \rho d\rho d\phi. \quad (2)$$

As before, in Eq. (2), the overall complex amplitude transmittance is denoted as  $P(\rho, \phi; \alpha)$ . We represent the cylindrical coordinates in the image domain as  $(r, \theta, z)$ . Since we use a small detector on-axis, we are interested in the complex amplitude distribution at  $r = 0$ . Then, Eq. (2) reduces to

$$p(0, \theta, z; \alpha) = 2\pi \int_0^\infty \langle P(\rho, \alpha) \rangle \exp\{-i\pi\lambda z \rho^2\} \rho d\rho. \quad (3)$$

In Eq. (3), we identify the following angular autocorrelation:

$$\langle P(\rho, \alpha) \rangle = \left\{ \frac{1}{2\pi} \int_0^{2\pi} P_1\left(\rho, \phi + \frac{\alpha}{2}\right) P_1\left(\rho, \phi - \frac{\alpha}{2}\right) d\phi \right\}. \quad (4)$$

In what follows, we exploit the above angular autocorrelation for describing an in-plane rotation sensor.

## 3. ANGULAR MASK WITH BARKER CODING

For the sake of clarity of our discussion, in what follows, we describe the designing steps for composing the proposed pair.

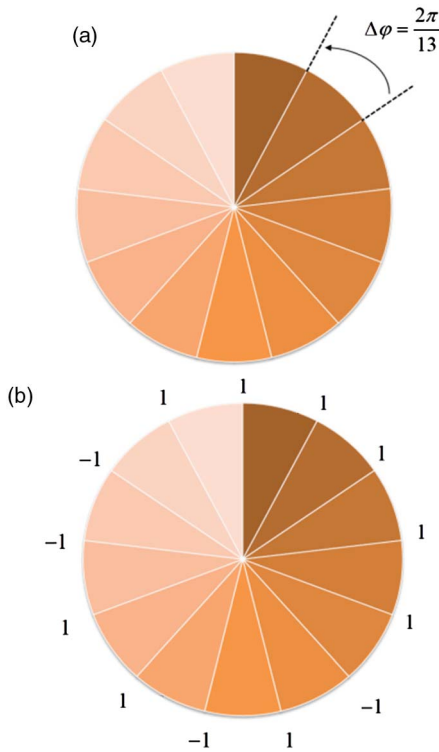


**Fig. 3.** Circular masks with radial narrow slits over an otherwise opaque support: (a) the slits are equiangular distributed; (b) each slit has a complex amplitude transmittance that is equal to the values of the Barker sequence of length  $L = 13$ .

In the first step, we consider that each mask has an integer number, say  $L$ , of radial narrow slits, as is depicted in Fig. 3. These radial slits are transparent over an otherwise opaque support. That is,

$$P_1(\rho, \phi) = \sum_{l=0}^{L-1} B_l \delta\left(\phi - \frac{l}{L} 2\pi\right) \text{circ}\left(\frac{\rho}{\Omega}\right). \quad (5)$$

In Eq. (5), the Latin letter  $B_l$  denotes the  $l$ th value of the Barker sequence of length  $L$ . The Dirac's delta represents the radial slits, which are angularly located at  $\phi = (l/L)2\pi$  for  $l = 0, 1 \dots L - 1$ . The mask is placed over a circular support, which is represented by the circular function,

$$\text{circ}\left(\frac{\rho}{\Omega}\right) = \begin{cases} 1 & \text{if } \rho \leq \Omega \\ 0 & \text{if } \rho > \Omega \end{cases}. \quad (6)$$

In Eq. (6), the Greek letter  $\Omega$  denotes the cutoff spatial frequency. It is rather intuitive to visualize that in the absence of an in-plane rotation ( $\alpha = 0$ ), the narrow slits of both masks coincide. Hence, the overall transmittance has a high value, which is proportional to the Barker length  $L$ .

If the set of slits of one mask is obstructed by the opaque regions of the other mask ( $0 < |\alpha| < 2\pi/L$ ), then the overall transmittance is zero.

Next, we note the following: if the rotation angle is  $|\alpha| = n(2\pi/L)$  for  $n = 1, 2 \dots L - 1$ , then Eq. (4) is equal to a minimum value. Except for the Barker sequence of length  $L = 4$ ,

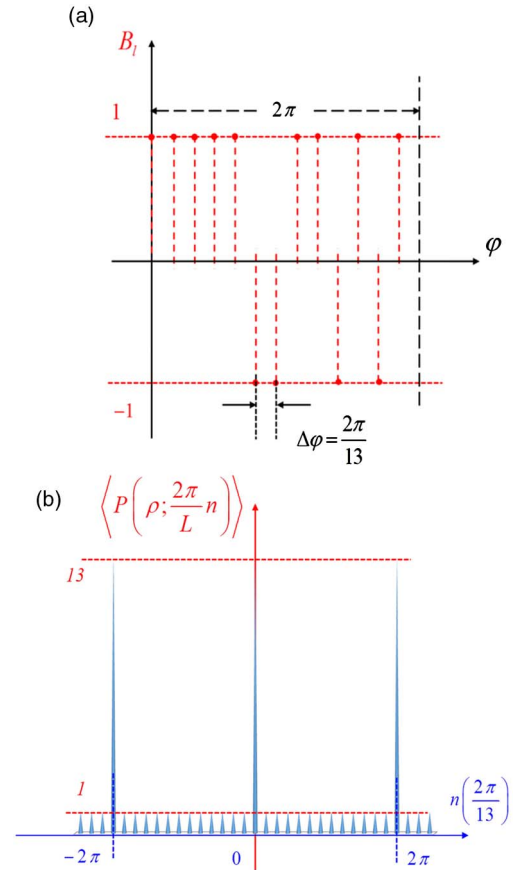


**Fig. 4.** Angular distributed radial slits and their angular autocorrelation: (a) Cartesian-like representation of the Barker sequence of length  $L = 13$ ; (b) the angular autocorrelation for in-plane rotations  $\alpha = n(2\pi/13)$  with  $n = 0, 1, 2, \text{ and } 3 \dots 13$ .

the minimum value is equal to  $-2, -1, 1, -1, -1, 1$  for the Barker sequence of lengths  $L = 2, 3, 5, 7, 11, 13$ , respectively.

As is depicted in Fig. 4, for this early design, we recognize that the whole operation described in Eq. (4) is the autocorrelation of the Barker sequence,

$$\left\langle P\left(\rho; \frac{2\pi}{L} n\right) \right\rangle = \frac{1}{2\pi} \sum_{m=0}^{L-1} B_{m+n} B_m \text{circ}\left(\frac{\rho}{\Omega}\right). \quad (7)$$

We note that by using narrow transparent slits over an otherwise opaque support, one generates a pair that has low light gathering power. Furthermore, the transition from the maximum correlation value to the minimum value happens until the misalignment angle is equal to  $(2\pi/L)$ . For  $L = 13$ , the misalignment angle is equal to  $27.69^\circ$ . This value of angular misalignment may be too high for some applications. For surpassing this limitation, we discuss, next, the final step of our design.

One can increase the sensitivity to angular misalignment or, equivalently one, can lower the tolerance to angular mismatch by using nested codes. One way of obtaining a nested code is to employ the direct product of the Barker sequence, which is commonly denoted as  $B_L \otimes B_L$ ; see, for example, Ref. [19]. The sequence associated with the direct product of the

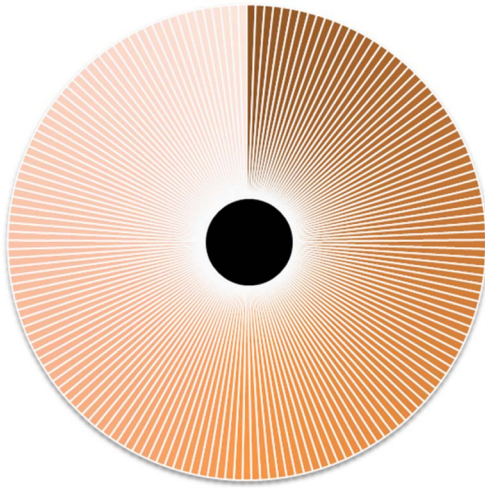


**Fig. 5.** Angular coding employing the direct product of the Barker sequence of length  $L = 13$ .

Barker sequence of length  $L$  has  $L \times L$  elements. The elements of the direct product of the Barker sequence of length 13 are

$$B_{13} \otimes B_{13} = \left\{ \begin{array}{l} 1, 1, 1, 1, 1, -1, -1, 1, 1, -1, 1, -1, 1, \\ 1, 1, 1, 1, 1, -1, -1, 1, 1, -1, 1, -1, 1, \\ 1, 1, 1, 1, 1, -1, -1, 1, 1, -1, 1, -1, 1, \\ 1, 1, 1, 1, 1, -1, -1, 1, 1, -1, 1, -1, 1, \\ 1, 1, 1, 1, 1, -1, -1, 1, 1, -1, 1, -1, 1, \\ -1, -1, -1, -1, -1, 1, 1, -1, -1, 1, 1, -1, -1, \\ -1, -1, -1, -1, -1, 1, 1, -1, -1, 1, 1, -1, -1, \\ 1, 1, 1, 1, 1, -1, -1, 1, 1, -1, 1, -1, 1, \\ 1, 1, 1, 1, 1, -1, -1, 1, 1, -1, 1, -1, 1, \\ -1, -1, -1, -1, -1, 1, 1, -1, -1, 1, 1, -1, -1, \\ 1, 1, 1, 1, 1, -1, -1, 1, 1, -1, 1, -1, 1, \\ -1, -1, -1, -1, -1, 1, 1, -1, -1, 1, 1, -1, -1, \\ 1, 1, 1, 1, 1, -1, -1, 1, 1, -1, 1, -1, 1 \end{array} \right\}. \quad (8)$$

In Fig. 5, we depict the 169 angular slits elements that are reported in Eq. (8).

For the nested Barker length of  $13 \times 13$ , the angular autocorrelation varies from 169 to 10. The drop occurs when the angular misalignment is equal to  $2\pi/169$ . If you will, the sensitivity to misalignment is  $(2.132)^\circ$ . This value may be useful for several applications. However, we note that in this paper we have failed to present a practical limit to the number of slits.

#### 4. FOCUS ERROR TOLERANCE

Next, we analyze the sensitivity of our proposal to errors caused by the location of the small size detector along the optical axis. To this end, it is convenient to normalize the irradiance distribution associated with the complex amplitude in Eq. (4). By taking into account the results in Eq. (7), we write the axial amplitude distribution in Eq. (3) as follows:

$$p(0, \theta, z; \alpha) = 2\pi \int_0^\infty \langle P(\rho, \alpha) \rangle \exp\{-i\pi\lambda z\rho^2\} \rho d\rho. \quad (9)$$

Now, except for the length  $L = 4$ , the generic formula for the angular autocorrelation is

$$\langle P(\rho; \alpha) \rangle = \frac{L}{2\pi} \left[ 1 - \left( 1 - \frac{\text{Min}}{L} \right) \left| \frac{L}{2\pi} \alpha \right| \right] \text{circ} \left( \frac{\rho}{\Omega} \right) \text{ if } |\alpha| \leq \frac{2\pi}{L}. \quad (10)$$

In Eq. (10), we denote as “Min” the minimum value of the angular autocorrelation. Except for  $L = 4$ , the minimum value is equal to  $-2, -1, 1, -1, -1, 1$  for the lengths  $L = 2, 3, 5, 7, 11, 13$ , respectively.

Next, for analyzing the influence of focus errors, in terms of the focus error coefficient  $W_{2,0}$ , it is convenient to employ the following change of variables:

$$\begin{aligned} \zeta &= \left( \frac{\rho}{\Omega} \right)^2 - \frac{1}{2}; \text{rect}(\zeta) = \text{circ} \left( \frac{\rho}{\Omega} \right); \\ W_{2,0} &= - \left( \frac{\lambda^2 \Omega^2}{2} \right) z; \\ q(\alpha; W_{2,0}) &= p(0, \theta, z; \alpha). \end{aligned} \quad (11)$$

By substituting Eq. (11) in Eq. (9) and after performing the integration, we obtain

$$\begin{aligned} q(\alpha; W_{2,0}) &= (\pi\Omega^2)L \left[ 1 - \left( 1 - \frac{\text{Min}}{L} \right) \left| \frac{L}{2\pi} \alpha \right| \right] \\ &\times \exp \left\{ i\pi \frac{W_{2,0}}{\lambda} \right\} \text{sinc} \left( \frac{W_{2,0}}{\lambda} \right). \end{aligned} \quad (12)$$

Now, for analyzing the sensitivity to angular mismatch and the tolerance to focus errors, we propose to use the square modulus of the normalized version of the complex amplitude distribution in Eq. (12). That is,

$$\begin{aligned} T(\alpha; W_{2,0}) &= \left| \frac{q(\alpha; W_{2,0})}{(\pi\Omega^2)L} \right|^2, \\ T(\alpha; W_{2,0}) &= \left[ 1 - \left( 1 - \frac{\text{Min}}{L} \right) \left| \frac{L}{2\pi} \alpha \right| \right]^2 \left[ \text{sinc} \left( \frac{W_{2,0}}{\lambda} \right) \right]^2, \\ &\text{if } |\alpha| \leq \frac{2\pi}{L}. \end{aligned} \quad (13)$$

We recognize that Eq. (13) is a new expression of the Strehl ratio versus focus errors, which is valid for the arbitrary Barker sequence of length  $L$ . This new formula has two independent factors. The first factor in Eq. (13) describes the changes of the angular autocorrelation as a function of the Barker length. This first factor is plotted in Fig. 6.

The second factor in Eq. (13) is the square of the cardinal sine function, which is identical to the Strehl ratio versus focus error of any imaging device, working at full pupil aperture.

From the result in Eq. (13), it is convenient to recognize the following: for angularly encoding a mask that has a high number of segments, it is convenient to have a central obscuration. Hence, it is relevant to analyze our proposed procedure when using annularly distributed masks. As is discussed in Appendix A, for annularly distributed masks with obscuration ratio  $\varepsilon$ , Eq. (13) becomes

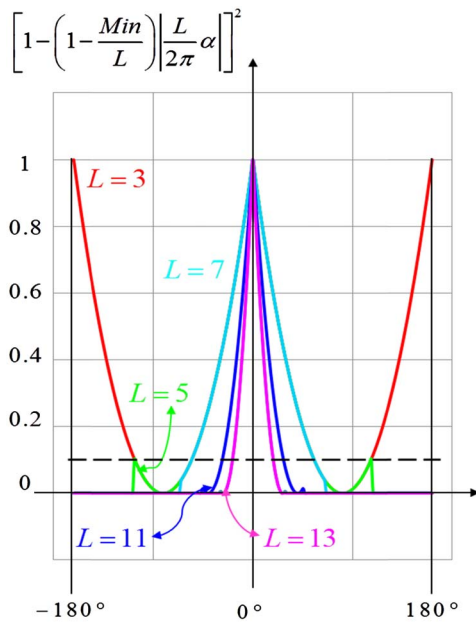


**Fig. 6.** Normalized versions of the angular autocorrelation for the variable Barker length. Along the horizontal axis, a black broken line represents a threshold value of 10% for avoiding the presence of white noise.

$$T(\alpha; W_{2,0}) = (1 - \epsilon^2)^2 \left[ 1 - \left( 1 - \frac{\text{Min}}{L} \right) \left| \frac{L}{2\pi} \alpha \right| \right]^2 \times \left[ \text{sinc} \left( (1 - \epsilon^2) \frac{W_{2,0}}{\lambda} \right) \right]^2. \tag{14}$$

It is clear from Eq. (14) that if one uses angular coded masks, which have a central obscuration, then the optical system has an increased tolerance to the focus error by the factor  $1/(1 - \epsilon^2)$ . However, we recognize that the central obscuration reduces the light gathering power by the factor  $(1 - \epsilon^2)^2$ .

### 5. POLARIZATION CODING SCHEME

In Fig. 7, we depict our proposal of using linearly polarized films for encoding, with high light throughput, the values of a Barker sequence of length  $L = 3$ . In Fig. 7(a), we use line arrows for depicting the positions of the three slits, while we employ boxed arrows for indicating the orientations of the linearly polarized films that cover the slits.

Two linearly polarized films (depicted as boxed arrows in red and in blue) are radially orientated. The remaining polarizer (depicted as a boxed arrow in black) is angularly orientated. Radial orientations represent the number one in the Barker sequence, while the angular orientation represents the number minus one in the Barker sequence.

In Fig. 7(b), we show the position changes of the slits, after introducing an in-plane rotation in steps of  $120^\circ$ . In Fig. 7(c), pairs of boxed arrows represent (at each slit) either crossed-polarization or polarization alignment.

It is apparent from Fig. 7 that by introducing an in-plane rotation of  $120^\circ$ , or of  $240^\circ$ , the angular correlation drops from the value of three to the value of one. Hence, for the polarized

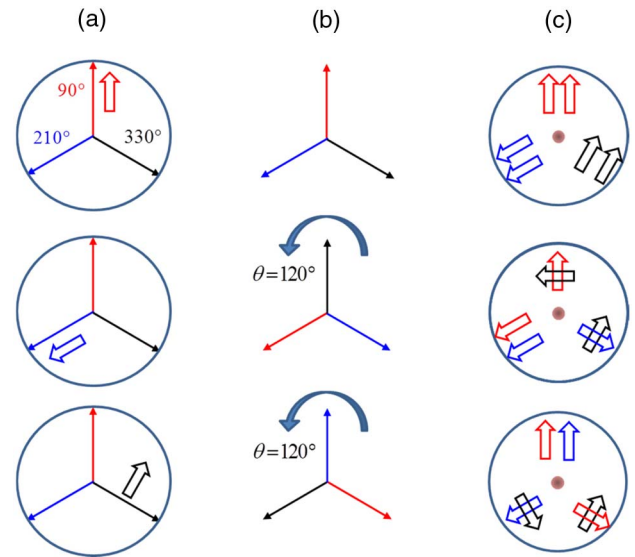


**Fig. 7.** On the left hand side, as line arrows, we display the position of the three slits on the mask, and, as boxed arrows, we depict the orientations of the linear polarizers. At the central column, we illustrate the position of the slits after in-plane rotations of  $120^\circ$ . At the right hand side, the boxed arrows depict either polarization alignment or crossed-polarization.

encoded masks, the ratios between the maxima and minima are not as high as the ratios of the original Barker sequences despite the fact that the polarization scheme provides a high light throughput.

As is depicted in Fig. 8, the ratio between the maxima and minima do not reach the expected values of the Barker sequences. However, the polarization scheme can be used with noncoherent light and for a rather wide chromatic spectral range.

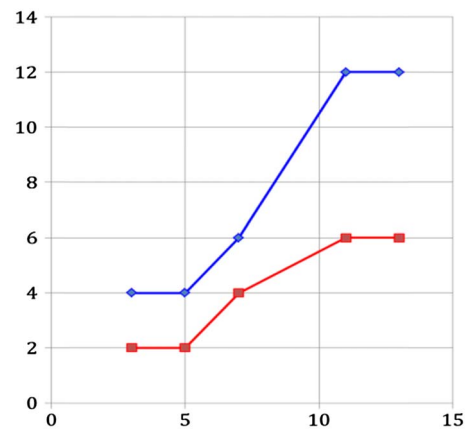


**Fig. 8.** Graphical display of the ratios between the maxima and the minima of the Barker sequence of length  $L = 3, 5, 7, 11,$  and  $13$ . (a) As a blue curve, we plot the ratios of the original Barker sequence. (b) As a red curve, we display the ratios for the polarization encoded versions. Further details of the polarization scheme are beyond our present scope. They will be published elsewhere. Next, we report preliminary experimental results of our proposals.

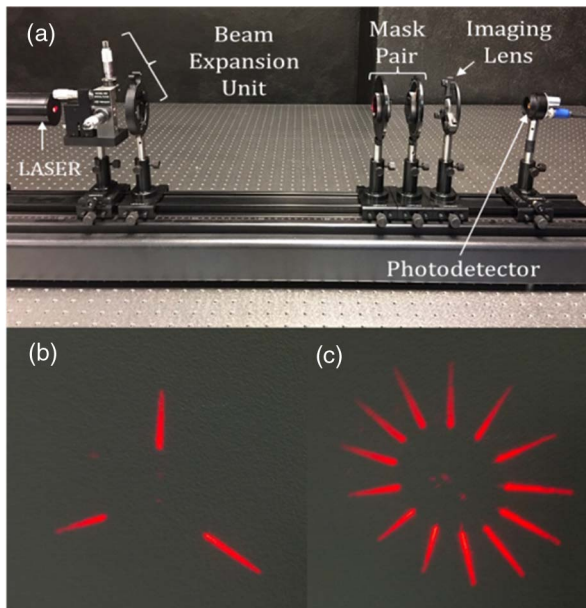


**Fig. 9.** Preliminary experiments: (a) The optical setup; (b) the irradiance distribution just behind the mask with 3 slits; and (c) the irradiance distribution with 13 slits.

## 6. PRELIMINARY EXPERIMENTAL VERIFICATIONS

In Fig. 9, we show the experimental setup for verifying the designs depicted in Fig. 3 for  $L = 3$  and  $L = 13$ .

A three-dimensional (3D) printer was used for generating (over otherwise uniform support) the required slits. The width of each slit is equal to  $1 \text{ mm} \pm 0.1 \text{ mm}$ , and the angular locations have errors of around 10% from the nominal values. As is apparent from Fig. 9, behind the masks, the diffraction spread is negligible.

In Fig. 10, we report the angular correlations that are obtained when employing clear slits (without polarization coding). From these preliminary experimental results, we claim that the angular correlations do exhibit narrow irradiance peaks. We also note that the maxima do not have the same values due to shape dissimilarities between the slits. Hence, the proposed technique can discriminate geometrical distortions on the masks.

In Fig. 11, we show the angular correlation if the proposed polarization coding is employed. We note that in this later case, the angular correlation has a high peak (with normalized irradiance distribution equal to unity) at  $\theta = 0^\circ$  and two peaks (with normalized irradiance distribution around the value equal to 0.3) at  $\theta = \pm 120^\circ$ . Again, the secondary peaks are different due to shape dissimilarities between the slits.

It is apparent from Fig. 11 that by using the polarization coding scheme, the angular correlation is able to discriminate well between the angular position  $\theta = 0^\circ$  and the angular position  $\theta = \pm 120^\circ$ . We obtain the above results using a He-Ne laser ( $\lambda = 623.8 \text{ nm}$ ), but we verify that similar results are also obtained with a broad band source.

Despite experimental limitations, the above preliminary results show that indeed one can obtain highly peaked angular correlations, which are able to discriminate either angular misalignments or the mask's shape distortions.

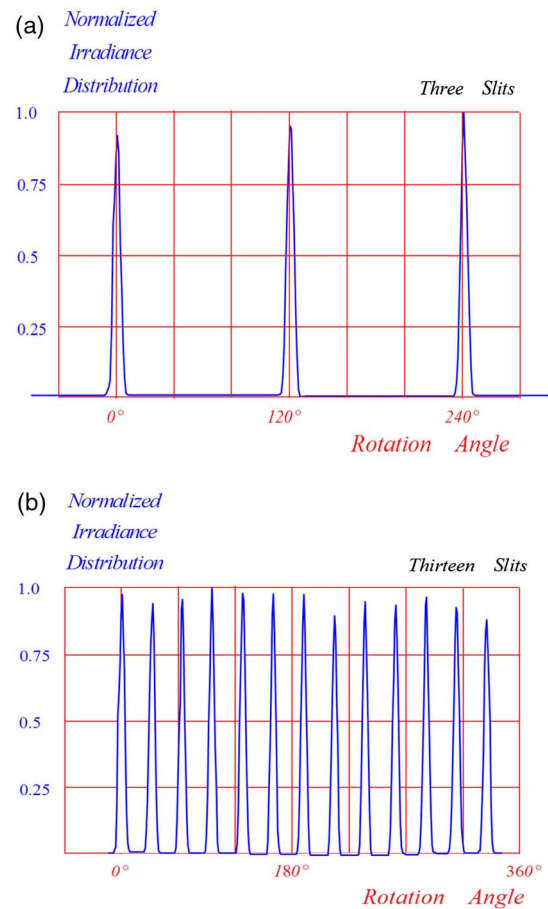


**Fig. 10.** Angular correlations obtained by using the optical setup in Fig. 9 and the masks in Fig. 3. For the experimental results in (a), we use three narrow slits. (b) The angular correlations are obtained using 13 slits.

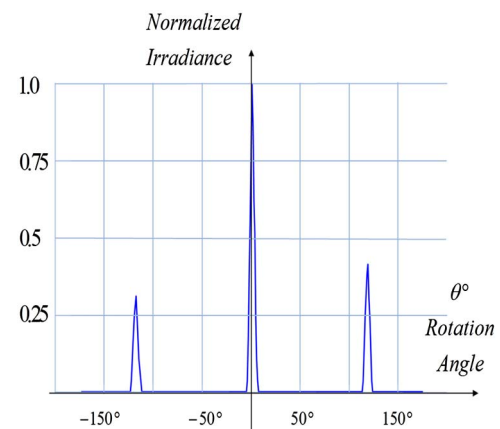


**Fig. 11.** Normalized angular correlation as a function of the rotation angle  $\theta$  if the pair of masks uses the polarization encoding scheme for the Barker sequence of length  $L = 3$ .

## 7. CONCLUSIONS

We have indicated that for testing the performance of varifocal lenses, it is desirable to have a technique for verifying that the

magnified images do not suffer from either geometrical distortions or in-plane rotations.

For the above tasks, we have noted that spindle patterns may be useful, since the images of these patterns have low dependence to lateral magnification.

We have shown that one can implement an angular correlator by employing a pair of suitably coded masks. We have discussed the designing steps for angularly encoding the masks forming the pair.

We have indicated that the proposed designs exploit the autocorrelation properties of the Barker sequence or pseudo-random sequence.

We have shown that the axial irradiance distribution reaches a maximum value if the elements of the composed pair are aligned. If there is an angular misalignment between the elements of the pair, then the axial irradiance distribution drops to a minimum value.

For the standard Barker sequence, the transition from the maximum to the minimum happens until the misalignment angle is equal to  $(2\pi/13)$ . If you will, it is equal to  $(27.69^\circ)$ . We have reported an analytical expression that relates the values of the angular autocorrelation versus angular misalignment.

We have proposed to use nested versions of the Barker code. We have shown that by using a nested Barker sequence, the transition from the maximum to the minimum happens if the misalignment angle is equal to  $(2\pi/169)$ . If you will, it is equal to  $(2.132^\circ)$ . We did not report any analytical formula for this case.

We have defined a merit function for describing the sensitivity of the method to focus errors. The merit function is a new expression of the Strehl ratio versus focus errors for an arbitrary Barker sequence of length  $L$ . The new formula has two independent factors. The first factor describes the changes of the angular autocorrelation as a function of the Barker length. The second factor is the square of the cardinal sine function, which is identical to the Strehl ratio versus focus error of any imaging device, working at full pupil aperture.

Our preliminary experimental results show that the angular correlations do generate narrow irradiance peaks. The variations on the values of the peaks are useful for identifying geometrical distortions of the slits. We have shown that the discrimination capabilities of the technique can be enhanced by coding the negative values and the positive values of a Barker sequence with linearly polarized films.

For the later task, we have indicated that the positive values of the Barker can be coded with linearly polarized light along the radial direction. The negative values of the Barker are coded with linearly polarized light along the angular direction.

As a proof of principle, we have verified experimentally the following result: for the Barker sequence of length  $L = 3$ , after in-plane rotations of  $120^\circ$ , the polarizing films produce either crossed-polarization or polarization alignment. Of course, this polarization coding scheme is not restricted to one particular case.

We have recognized that despite the fact that the polarization scheme provides a high light throughput, the ratios between the maxima and the minima are not as high as the

ratios of the original Barker sequences. However, our polarization coding can be used with broad band noncoherent sources.

## APPENDIX A

If the support has a central obscuration, then instead of using the Eq. (5) in the main text, we use the following amplitude transmittance:

$$P_1(\rho; \phi) = \sum_{l=0}^{L-1} B_l \text{rect}\left(\frac{\phi - \frac{l}{L}2\pi}{\frac{2\pi}{L}}\right) \left[ \text{circ}\left(\frac{\rho}{\Omega}\right) - \text{circ}\left(\frac{\rho}{\varepsilon\Omega}\right) \right]. \tag{A1}$$

In Eq. (A1), the Greek letter  $\varepsilon$  is a dimensionless, real positive number, such that  $0 < \varepsilon < 1$ . This dimensionless number scales the obscuration ratio in terms of the maximum radius  $\Omega$ . In mathematical terms, the inner circle is

$$\text{circ}\left(\frac{\rho}{\varepsilon\Omega}\right) = \begin{cases} 1 & \text{if } \varepsilon\Omega \leq \rho \leq \Omega \\ 0 & \text{otherwise} \end{cases}. \tag{A2}$$

Next, we note that for describing the axial amplitude distribution of the annular support, it is convenient to modify the change of variables in Eq. (A1). Now, we have that

$$\zeta = \frac{1}{1 - \varepsilon^2} \left[ \left(\frac{\rho}{\Omega}\right)^2 - \varepsilon^2 \right] - \frac{1}{2},$$

$$\text{rect}(\zeta) = \text{circ}\left(\frac{\rho}{\Omega}\right) - \text{circ}\left(\frac{\rho}{\varepsilon\Omega}\right),$$

$$W_{2,0} = -\left(\frac{\lambda^2\Omega^2}{2}\right)z,$$

$$q(\alpha; W_{2,0}) = p(0, \theta, z; \alpha). \tag{A3}$$

Trivially, for  $\varepsilon = 0$ , Eq. (A3) reduces to Eq. (A1). By substituting Eq. (A3) in Eq. (14), and after performing the integration, we obtain

$$q(\alpha; W_{2,0}) = (1 - \varepsilon^2)(\pi\Omega^2)$$

$$\times L \left[ 1 - \left(1 - \frac{Min}{L}\right) \left| \frac{L}{2\pi} \alpha \right| \right]$$

$$\times \exp \left\{ i\pi(1 + \varepsilon^2) \left(\frac{W_{2,0}}{\lambda}\right) \right\}$$

$$\times \text{sinc} \left( (1 - \varepsilon^2) \frac{W_{2,0}}{\lambda} \right). \tag{A4}$$

Now, the square modulus of the normalized version of the complex amplitude distribution in Eq. (A4) reads

$$T(\alpha; W_{2,0}) = (1 - \varepsilon^2)^2 \left[ 1 - \left(1 - \frac{Min}{L}\right) \left| \frac{L}{2\pi} \alpha \right| \right]^2$$

$$\times \left[ \text{sinc} \left( (1 - \varepsilon^2) \frac{W_{2,0}}{\lambda} \right) \right]^2. \tag{A5}$$

Equation (A5) is Eq. (A4) in the main text.

**Acknowledgment.** The authors are indebted to Eduardo Aguilera-Gomez and Hector Plascencia-Mora for producing the masks, which are used in our preliminary experimental results.

## REFERENCES

- B. Berge and J. Peseux, "Variable focal lens controlled by an external voltage: an application of electrowetting," *Eur. Phys. J. E* **3**, 159–163 (2000).
- H. W. Ren, Y. H. Fan, S. Gauza, and S. T. Wu, "Tunable-focus flat liquid crystal spherical lens," *Appl. Phys. Lett.* **84**, 4789–4791 (2004).
- D. Y. Zhang, N. Justis, and Y. H. Lo, "Fluidic adaptive zoom lens with high zoom ratio and widely tunable field of view," *Opt. Commun.* **249**, 175–182 (2005).
- B. H. W. Hendriks, S. Kuiper, M. A. J. Van As, C. A. Renders, and T. W. Tukker, "Electrowetting-based variable-focus lens for miniature systems," *Opt. Rev.* **12**, 255–259 (2005).
- M. Duocastella and C. B. Arnold, "Enhanced depth of field laser processing using an ultrahigh-speed axial scanner," *Appl. Phys. Lett.* **102**, 061113 (2013).
- A. N. Simonov and G. Vdovin, "Cubic optical elements for an accommodative intraocular lens," *Opt. Express* **14**, 7757–7775 (2006).
- J. Schwiegerling and C. Paleta-Toxqui, "Minimal movement zoom lens," *Appl. Opt.* **48**, 1932–1935 (2009).
- A. Mikš and J. Novák, "Analysis of two-element zoom systems based on variable power lenses," *Opt. Express* **18**, 6797–6810 (2010).
- A. Mikš and J. Novák, "Three-component double conjugate zoom lens system from tunable focus lenses," *Appl. Opt.* **52**, 862–865 (2013).
- J. Ojeda-Castaneda, C. M. Gómez-Sarabia, and S. Ledesma, "Novel zoom systems using a vortex pair," *Asian J. Phys.* **23**, 415–424 (2014).
- R. H. Barker, *Communication Theory*, W. Jackson, ed. (Academic, 1953), p. 273.
- K. Patorski and M. Kujawska, *The Handbook of the Moiré Fringe Technique* (Elsevier, 1993).
- I. Amidror, *The Theory of the Moiré Phenomenon: Periodic Layers* (Springer, 2009).
- R. Hanbury Brown and R. Q. Twiss, "A test of a new type of stellar interferometer on sirius," *Nature* **178**, 1046–1048 (1956).
- E. Klotz and M. Kock, "A simple ground-glass correlator," *Opt. Commun.* **6**, 391–393 (1964).
- H. M. Pedersen, "Intensity correlation metrology: a comparative study," *Opt. Acta* **29**, 105–118 (1982).
- M. A. Sutton, J.-J. Orteu, and H. W. Schreier, *Image Correlation for Shape, Motion and Deformation Measurements* (Springer, 2009).
- J. Tzai, S. C. C. Hsu, H. Chen, C. Chen, Y. C. Pai, C.-C. Yu, C. C. Lin, T. Itzkovich, L. Yap, E. Amit, D. Tien, E. Huang, K. T. L. Kuo, and N. Amir, "Techniques for improving overlay accuracy by using device correlated metrology targets as reference," *J. Micro/Nanolithogr. MEMS MOEMS* **13**, 041412 (2014).
- N. Levanon and E. Mozeson, *Radar Signals*, 1st ed. (Wiley, 2004), pp. 107–113.
- R. H. Katyl, "Moiré screens coded with pseudo-random sequences," *Appl. Opt.* **11**, 2278–2285 (1972).
- J. Ojeda-Castañeda and J. Carranza, "Moiré with zone plates pseudo-randomly encoded," *Opt. Commun.* **97**, 157–161 (1993).
- A. Saucedo-Carvajal and J. Ojeda-Castaneda, "Random gratings as correlator sensors," *Opt. Lett.* **22**, 257–258 (1997).
- J. Ojeda-Castaneda, L. Díaz-Santana, and J. Piñataro, "Pseudorandom gratings for noncoherent theta-decoders," *Opt. Commun.* **157**, 209–217 (1998).
- E. M. Granger, "Electronic graphic arts screener that suppresses moiré patterns using pseudo-random font selection," U.S. patent 4,916,545 (10 April 1990).
- Y. Zhou, H. Fan, S. An, J. Li, J. Wang, J. Zhou, and Y. Liu, "Pseudo-random arranged color filter array for controlling moiré patterns in display," *Opt. Express* **23**, 29390–29398 (2015).
- J. A. Tropp, J. N. Laska, M. F. Duarte, J. K. Romberg, and R. G. Baraniuk, "Beyond Nyquist: efficient sampling of sparse bandlimited signals," *IEEE Trans. Inf. Theory* **56**, 520–544 (2010).
- J. M. Nichols and F. Bucholtz, "Beating Nyquist with light: a compressively sampled photonic link," *Opt. Express* **19**, 7339–7348 (2011).
- C. W. McCutchen, "Generalized aperture and the three-dimensional diffraction image," *J. Opt. Soc. Am.* **54**, 240–244 (1964).
- J. Ojeda-Castaneda and C. M. Gómez-Sarabia, "Tuning field depth at high resolution by pupil engineering," *Adv. Opt. Photon.* **7**, 814–824 (2015).